arXiv:1608.04678v1 [cond-mat.mes-hall] 16 Aug 2016

Quantum oscillations without magnetic field

Tianyu Liu, D. I. Pikulin, and M. Franz
Department of Physics and Astronomy, University of British Columbia, Vancouver, BC, Canada V6T 1Z1 and Quantum Matter Institute, University of British Columbia, Vancouver BC, Canada V6T 1Z4
(Dated: August 17, 2016)

When magnetic field B is applied to a metal, nearly all observable quantities exhibit oscillations periodic in $1/B$. Such quantum oscillations reflect the fundamental reorganization of electron states into Landau levels as a canonical response of the metal to the applied magnetic field. We predict here that, remarkably, in the recently discovered Dirac and Weyl semimetals quantum oscillations can occur in the complete absence of magnetic field. These zero-field quantum oscillations are driven by elastic strain which, in the space of the low-energy Dirac fermions, acts as a chiral gauge potential. We propose an experimental setup in which the strain in a thin film (or nanowire) can generate pseudomagnetic field b as large as 15T and demonstrate the resulting de Haas-van Alphen and Shubnikov-de Haas oscillations periodic in $1/b$.

Dirac and Weyl semimetals [1–3] are known to exhibit a variety of exotic behaviors owing to their unusual electronic structure comprised of linearly dispersing electron bands at low energies. This includes the pronounced negative magnetoresistance [4–11] attributed to the phenomenon of the chiral anomaly [12–14], theoretically predicted nonlocal transport [15, 16], Majorana flat bands [17], as well as an unusual type of quantum oscillations (QO) that involve both bulk and topologically protected surface states [18, 19]. In this theoretical study we establish a completely new mechanism for QO in Dirac and Weyl semimetals that requires no magnetic field. These zero-field oscillations occur as a function of the applied elastic strain and, similar to the canonical de Haas-van Alphen and Shubnikov-de Haas oscillations [20], manifest themselves as oscillations periodic in $1/b$, where b is the strain-induced pseudomagnetic field, in all measurable thermodynamic and transport properties. To the best of our knowledge this is the first instance of such zero-field quantum oscillations in any known substance.

Materials with linearly dispersing electrons respond in peculiar ways to the externally imposed elastic strain. In graphene, for instance, the effect of curvature is famously analogous to a pseudomagnetic field [21] that can be quite large and is known to generate pronounced Landau levels observed in the tunneling spectroscopy [22]. Recent theoretical work [23–27] showed that similar effects can be anticipated in three-dimensional Dirac and Weyl semimetals, although the estimated field strengths in the geometries that have been considered are rather small (below 1 Tesla in Ref. [26]). Ordinary quantum oscillations, periodic in $1/B$, have already been observed in Dirac semimetals Cd_3As_2 and Na_3Bi [19, 28–30] but the magnetic field required is $B \gtrsim 2$T. This, then, would seem to rule out the observation of strain-induced QO in geometries considered previously. We make a key advance in this work by devising a new geometry in which pseudomagnetic field b as large as 15T can be achieved. The proposed setup consists of a thin film (or a nanowire) in which pseudomagnetic field b is generated by a simple bend as illustrated in Fig. 1.

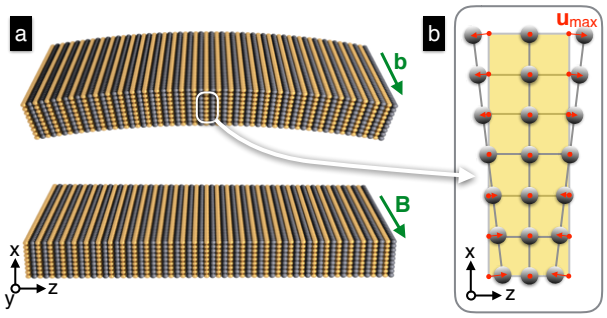

FIG. 1: Proposed setup for strain-induced quantum oscillation observation in Dirac and Weyl semimetals. a) Bent film is analogous, in terms of its low-energy properties, to an unstrained film subject to magnetic field B. b) Detail of the atomic displacements in the bent film. Displacements have been exaggerated for clarity.

For simplicity and concreteness we focus in the following on Dirac semimetal Cd_3As_2 [28, 31–35] which is the best characterized representative of this class of materials. Our results are directly applicable also to Na_3Bi [36–38] whose low-energy description is identical, and are easily extended to other Dirac and Weyl semimetals [39–43]. We start from the tight-binding model formulated in Refs. [31, 36] which describes the low-energy physics of Cd_3As_2 by including the band inversion of its atomic Cd-5s and As-4p levels near the Γ point. In the basis of the spin-orbit coupled states $|P_{\frac{3}{2}}, \frac{3}{2}\rangle$, $|S_{\frac{1}{2}}, \frac{1}{2}\rangle$, $|S_{\frac{1}{2}}, -\frac{1}{2}\rangle$ and $|P_{\frac{3}{2}}, -\frac{3}{2}\rangle$ the model is defined by a 4×4 matrix Hamiltonian

$$H^{\rm latt} = \epsilon_{\boldsymbol{k}} + \begin{pmatrix} h^{\rm latt} & 0 \\ 0 & -h^{\rm latt} \end{pmatrix}, \qquad (1)$$

on a simple rectangular lattice with spacings $a_{x,y,z}$, where

$$h^{\rm latt}(\boldsymbol{k}) = m_{\boldsymbol{k}}\tau^z + \Lambda(\tau^x \sin a_x k_x + \tau^y \sin a_y k_y), \qquad (2)$$

$\boldsymbol{\tau}$ are Pauli matrices in the orbital space and $m_{\boldsymbol{k}} = t_0 + t_1 \cos a_z k_z + t_2(\cos a_x k_x + \cos a_y k_y)$. For the analytic calculations below we will assume $a_i = a$, while

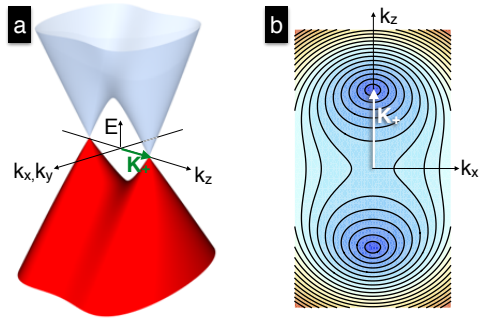

FIG. 2: Schematic depiction of the low-energy electron excitation spectrum in Dirac and Weyl semimetals. a) In a Dirac semimetal the bands are doubly degenerate due to the spin degree of freedom while in a Weyl semimetal they are non-degenerate. b) Contours of constant energy for $k_y = 0$. For magnetic field $\boldsymbol{B} \parallel \hat{y}$ these correspond to the extremal orbits [20] that give rise to QO periodic in $1/B$.

in numerics we will use the actual lattice constants of Cd_3As_2. Various tunneling amplitudes and $\epsilon_{\boldsymbol{k}}$ are given in Supplementary Material (SM). The low-energy spectrum of $h^{\rm latt}$ consists of a pair of Weyl points, shown in Fig. 2a, which carry opposite chirality $\eta = \pm 1$ and are located at crystal momenta $\boldsymbol{K}_\eta = (0, 0, \eta Q)$ with Q given by $\cos(aQ) = -(t_0+2t_2)/t_1$. The lower diagonal block in Eq. (1) describes the spin-down sector in Cd_3As_2 and has identical spectrum. Terms in $\epsilon_{\boldsymbol{k}}$ account for particle-hole (p-h) asymmetry present in Cd_3As_2.

Following Refs. [23–26] the most important effect of elastic strain can be included in the lattice model (1) by modifying the electron tunneling amplitude along the $\hat{z}$-direction according to

$$t_1\tau^z \to t_1(1-u_{33})\tau^z + i\Lambda\sum_{j\neq 3} u_{3j}\tau^j, \qquad (3)$$

where $u_{ij} = \frac{1}{2}(\partial_i u_j + \partial_j u_i)$ is the symmetrized strain tensor and $\boldsymbol{u} = (u_1, u_2, u_3)$ represents the displacement of the atoms. To see how this leads to an emergent vector potential we study the low-energy effective theory. We expand $h^{\rm latt}(\boldsymbol{k})$ in the vicinity of the Weyl points $\boldsymbol{K}_\pm$ by writing $\boldsymbol{k} = \boldsymbol{K}_\pm + \boldsymbol{q}$ and assuming small $|\boldsymbol{q}|$. To leading order we obtain the linearized Hamiltonian of the distorted crystal [26]

$$h_\eta(\boldsymbol{q}) = v_\eta^j \tau^j \left(\hbar q_j - \eta\frac{e}{c}\mathcal{A}_j\right), \qquad (4)$$

with the velocity vector

$$\boldsymbol{v}_\eta = \hbar^{-1}a(\Lambda, \Lambda, -\eta t_1 \sin aQ). \qquad (5)$$

For Cd_2As_3 parameters and lattice constant $a = 4$Å this gives $\hbar\boldsymbol{v}_\eta = (0.89, 0.89, -1.24\eta)$eVÅ. The strain-induced gauge potential is given by

$$\vec{\mathcal{A}} = -\frac{\hbar c}{ea}\big(u_{13}\sin aQ, u_{23}\sin aQ, u_{33}\cot aQ\big). \qquad (6)$$

We see that elements u_{j3} of the strain tensor act on the low-energy Weyl fermions as components of a chiral gauge field because according to Eq. (4) $\vec{\mathcal{A}}$ couples with the opposite sign to the Weyl fermions with opposite chirality η. Ordinary electromagnetic gauge potential couples through the replacement $\hbar\boldsymbol{q} \to \hbar\boldsymbol{q} - \frac{e}{c}\boldsymbol{A}$, independent of η. Ref. [26] noted that application of a torsional strain to a nanowire made of Cd_3As_2 (grown along the 001 crystallographic direction) results in a uniform pseudomagnetic field $\boldsymbol{b} = \nabla \times \vec{\mathcal{A}}$ pointed along the axis of the wire. The strength of this pseudomagnetic field was estimated as $b \lesssim 0.3$T which would be insufficient to observe QO. Our key observation here is that a different type of distortion, illustrated in Fig. 1a, can produce a much larger field b.

One reason why the torsion-induced b-field is relatively small lies in the fact that it originates from the $\mathcal{A}_x$ and $\mathcal{A}_y$ components of the vector potential. According to Eq. (6) these are suppressed relative to the strain components by a factor of $\sin aQ$. This is a small number in most Dirac and Weyl semimetals because the distance $2Q$ between the Weyl points is typically a small fraction of the Brillouin zone size $2\pi/a$. Specifically, we have $aQ \simeq 0.132$ in Cd_3As_2 [31]. Note on the other hand that the $\mathcal{A}_z$ component of the chiral gauge potential comes with a factor $\cot aQ \simeq 1/aQ$ and is therefore enhanced. A lattice distortion that produces nonzero strain tensor element u_{33} will therefore be much more efficient in generating large b than u_{13} or u_{23}. Specifically, for the same amount of strain the field strength is enhanced by a factor of $\cot aQ/\sin aQ \simeq 1/(aQ)^2 \simeq 57$ for Cd_3As_2.

To implement this type of strain we consider a thin film (or a nanowire) grown such that vector $\boldsymbol{K}_\eta$ lies along the z direction as defined in Fig. 1a. More generally we require that $\boldsymbol{K}_\eta$ has a nonzero projection onto the surface of the film or on the long direction for the nanowire. Cd_3As_2 films [29], microribbons [44] and nanowires [45, 46] satisfy this requirement. Bending the film as shown in Fig. 1b creates a displacement field $\boldsymbol{u} = (0, 0, 2\alpha xz/d)$, where d is the film thickness and α controls the magnitude of the bend. (If R is the radius of the circular section formed by the bent film then $\alpha = 2d/R$. α can also be interpreted as the maximum fractional displacement $\alpha = u_{\rm max}/a$ that occurs at the surface of the film.) This distortion gives $u_{33} = 2\alpha x/d$ which, through Eq. (6), yields a pseudomagnetic field

$$\boldsymbol{b} = \nabla \times \vec{\mathcal{A}} = \hat{y}\left(\frac{2\alpha}{d}\right)\frac{\hbar c}{ea}\cot aQ. \qquad (7)$$

Noting that $\Phi_0 = hc/e = 4.12 \times 10^5$TÅ we may estimate the resulting field strength for a $d = 100$nm film as

$$b \simeq \alpha \times 246\text{T}. \qquad (8)$$

The maximum pseudomagnetic field that can be achieved will depend on the maximum strain that the material can

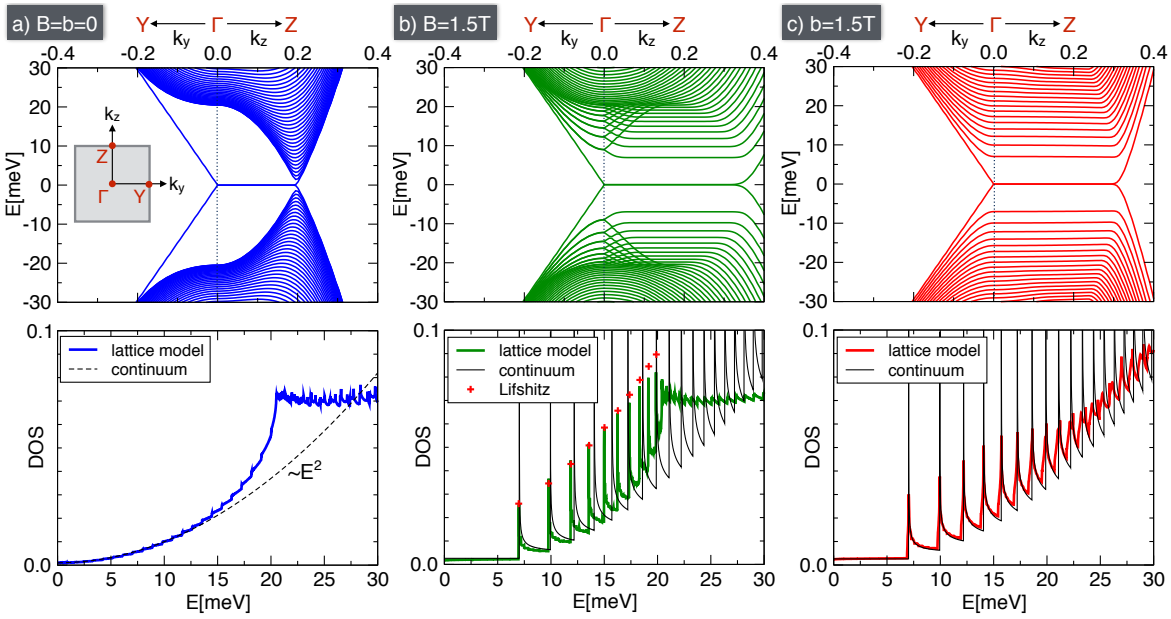

FIG. 3: Numerical results for the Cd_3As_2 lattice Hamiltonian (2) in the presence of magnetic field $\boldsymbol{B} = \hat{y}B$ and strain-induced pseudomagnetic field $\boldsymbol{b} = \hat{y}b$. In all panels films of thickness 500 lattice points are studied with parameters appropriate for Cd_3As_2. P-h asymmetry terms $\epsilon_{\boldsymbol{k}}$ are neglected for simplicity which makes contributions from the two spin sectors identical. a) Band structure and density of states (DOS) for zero field and zero strain. The inset shows the first Brillouin zone. b) Band structure and normalized DOS for $B = 1.5$T. Red crosses indicate the peak positions expected on the basis of the Lifshitz-Onsager quantization condition [20]. c) Band structure and DOS for $b = 1.5$T. Thin black line shows the expected bulk DOS for ideal Weyl dispersion computed from Eq. (9).

sustain. Ref. [45] characterized the Cd_3As_2 nanowires as "greatly flexible" and their Figure 1a shows some wires bent with a radius R as small as several microns. This implies that α of several percent can likely be achieved. From Eq. (8) we thus estimate that field strength $b \simeq 10-15$T can be reached, providing a substantial window for the observation of the strain-induced QO.

To substantiate these claims we now present the results of our numerical simulations based on the lattice Hamiltonian (2). Magnetic field B is implemented via the standard Peierls substitution while the strain-induced field b through Eq. (3). Geometry outlined in Fig. 1 is used with periodic boundary conditions along y and z, open along x. Fig. 3 provides the summary of our results. The unstrained crystal at zero field (panel a) shows the expected band structure with bulk Weyl nodes close to $k_z a = \pm 0.2$ and a pair of linearly dispersing surface states corresponding to Fermi arcs. The density of states (DOS) exhibits the expected quadratic behavior $D(E) \sim E^2$ at low energies with some deviations apparent for $|E| \gtrsim 12$meV due to the departure of the lattice model from the perfectly linear Weyl dispersion. At $E_{\rm Lif} \simeq 20$meV Lifshitz transition occurs where two small Fermi surfaces associated with each Weyl point merge into a single large Fermi surface as illustrated in Fig. 2b.

In Fig. 3b magnetic field $\boldsymbol{B} = \hat{y}B$ is seen to reorganize the linearly dispersing bulk bands into flat Landau levels. In the continuum approximation given by Eq. (4) the bulk spectrum of such Dirac-Landau levels is well known and reads

$$E_n(k_y) = \pm\hbar\sqrt{v_y^2 k_y^2 + 2n v_x v_z \frac{e|B|}{\hbar c}}, \quad n = 1, 2, \ldots, \quad (9)$$

The corresponding DOS shows a series of spikes at the onset of each new Landau level and is in a good agreement with the DOS calculated from the lattice model. Deviations occur above ~ 12meV because the energy dispersion of the lattice model is no longer perfectly linear at higher energies. The peak positions E_n agree perfectly with the Lifshitz-Onsager quantization condition [20], which takes into account these deviations. It requires that $S(E_n) = 2\pi n(eB/\hbar c)$, where $S(E)$ is the extremal cross-sectional area of a surface of constant energy E in the plane perpendicular to $\boldsymbol{B}$ (see Fig. 2b), and $n = 1, 2, \cdots$.

Pseudomagnetic field $\boldsymbol{b} = \hat{y}b$, induced by strain using Eq. (3) with $u_{33} = 2\alpha x/d$, also generates flat bands (panel c), as expected on the basis of arguments presented above. The corresponding DOS is in agreement with that obtained from Eq. (9) upon replacing $B \to b$. Remarkably the agreement is nearly perfect for all energies up to $E_{\rm Lif}$. We attribute this interesting result to the fact that strain couples as the chiral vector potential *only* to the Weyl fermions. If we write the full Hamiltonian as $h(\boldsymbol{p}) = h_W(\boldsymbol{p}) + \delta h(\boldsymbol{p})$ where h_W is strictly linear

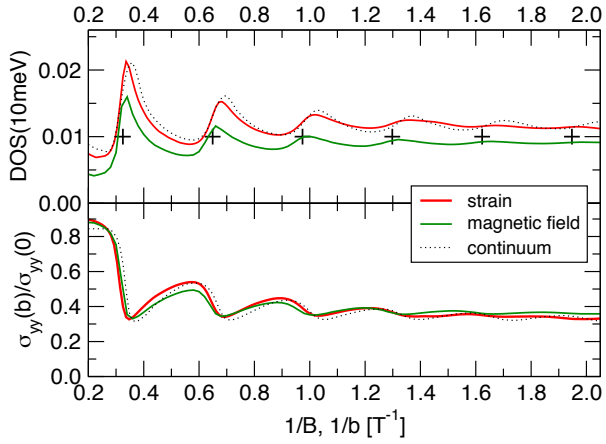

FIG. 4: Strain-induced QO. Top pannel shows oscillations in DOS at energy 10meV as a function of inverse strain strength expressed as $1/b$. For comparison ordinary magnetic oscillations are displayed, as well as the result of the bulk continuum theory Eq. (9). Crosses indicate peak positions expected based on the Lifshitz-Onsager theory. Bottom pannel shows oscillations in conductivity σ_{yy} assuming Fermi energy $E_F = 10$meV. To simulate the effect of disorder all data are broadened by convolving in energy with a Lorentzian with width $\delta = 0.25$meV. The same geometry and parameters are used as in Fig. 3.

in momentum $\boldsymbol{p}$ and δh is the correction resulting from the lattice effects, then strain causes $\boldsymbol{p} \to \boldsymbol{p} - \frac{e}{c}\vec{A}$ only in h_W but does not to leading order affect δh. The real vector potential $\boldsymbol{A}$ affects h_W and δh in the same way.

These results imply that QO will occur when either B or b is present. If we vary B then $D(E_F)$, together with most measurable quantities, will exhibit oscillations periodic in $1/B$. The same is true for the strain-induced pseudomagnetic field b. This is illustrated in Fig. 4 which shows oscillations in DOS and longitudinal conductivity σ_{yy} at energy 10meV as a function of $1/b$ and $1/B$. Conductivity is calculated using the standard relaxation time approximation as described in SM. Strain-induced QO show robust periodicity in $1/b$. Their period $0.329\mathrm{T}^{-1}$ is in a good agreement with the period $0.324\mathrm{T}^{-1}$ expected on the basis of the Lifshitz-Onsager theory and $0.336\mathrm{T}^{-1}$ obtained from Eq. (9). Small irregularities that appear at low fields can be attributed to the finite size effects as the Landau level spacing becomes comparable to the subband spacing apparent e.g. in Fig. 3a. We verified that similar oscillations occur at other energies below the Lifshitz transition. Remarkably, we find strain-induced oscillations periodic in $1/b$ also above E_{Lif}. In addition, we expect that in the presence of both b and B fields the peaks split as two Weyl cones feel different effective magnetic fields. These effects are further discussed in SM.

Results presented above extend trivially to the full Cd_3As_2 Hamiltonian Eq. (1) where the spin-down block makes an identical contribution and the p-h symmetry breaking terms contained in $\epsilon_{\boldsymbol{k}}$ bring only quantitative changes (see SM for discussion). Experimental studies [32–35] indicate that the linear dispersion in Cd_3As_2 extends over a much wider range of energies than theoretically anticipated [31] with the Lifshitz transition occurring above ~ 200meV. We therefore expect the zero-field strain-induced QO predicted in this work to be easily observable in suitably fabricated Cd_3As_2 films and nanowires and potentially also in other Dirac and Weyl semimetals. Our results show that conditions for their observability are identical to those required to detect ordinary QO. The continuous tunability of the pseudomagnetic field in large parameter range provides a new experimental basis for the study of emergent gauge fields in three-dimensional crystalline solids.

The authors are indebted to D.A. Bonn, D.M. Broun, A. Chen, I. Elfimov and W. N. Hardy for illuminating discussions, and thank NSERC, CIfAR and Max Planck - UBC Centre for Quantum Materials for support.

[1] X. Wan, A. M. Turner, A. Vishwanath, and S. Y. Savrasov, Phys. Rev. B **83**, 205101 (2011).
[2] A. A. Burkov, M. D. Hook, and L. Balents, Phys. Rev. B **84**, 235126 (2011).
[3] O. Vafek and A. Vishwanath, Annual Review of Condensed Matter Physics **5**, 83 (2014).
[4] K. Fukushima, D. E. Kharzeev, and H. J. Warringa, Phys. Rev. D **78**, 074033 (2008).
[5] D. T. Son and B. Z. Spivak, Phys. Rev. B **88**, 104412 (2013).
[6] H.-J. Kim, K.-S. Kim, J.-F. Wang, M. Sasaki, N. Satoh, A. Ohnishi, M. Kitaura, M. Yang, and L. Li, Phys. Rev. Lett. **111**, 246603 (2013).
[7] X. Huang, L. Zhao, Y. Long, P. Wang, D. Chen, Z. Yang, H. Liang, M. Xue, H. Weng, Z. Fang, et al., Phys. Rev. X **5**, 031023 (2015).
[8] J. Xiong, S. K. Kushwaha, T. Liang, J. W. Krizan, M. Hirschberger, W. Wang, R. J. Cava, and N. P. Ong, Science **350**, 413 (2015).
[9] A. A. Burkov, Journal of Physics: Condensed Matter **27**, 113201 (2015).
[10] Q. Li, D. E. Kharzeev, C. Zhang, Y. Huang, I. Pletikosic, A. V. Fedorov, R. D. Zhong, J. A. Schneeloch, G. D. Gu, and T. Valla, Nat Phys **12**, 550 (2016).
[11] C.-L. Zhang, S.-Y. Xu, I. Belopolski, Z. Yuan, Z. Lin, B. Tong, G. Bian, N. Alidoust, C.-C. Lee, S.-M. Huang, et al., Nat Commun **7**, 10735 (2016).
[12] S. L. Adler, Phys. Rev. **177**, 2426 (1969).
[13] J. S. Bell and R. Jackiw, Il Nuovo Cimento A (1971-1996) **60**, 47 (1969).
[14] H. Nielsen and M. Ninomiya, Physics Letters B **130**, 389 (1983).
[15] S. A. Parameswaran, T. Grover, D. A. Abanin, D. A. Pesin, and A. Vishwanath, Phys. Rev. X **4**, 031035 (2014).
[16] Y. Baum, E. Berg, S. A. Parameswaran, and A. Stern, Phys. Rev. X **5**, 041046 (2015).

[17] A. Chen and M. Franz, Phys. Rev. B **93**, 201105 (2016).
[18] A. C. Potter, I. Kimchi, and A. Vishwanath, Nat Commun **5**, 5161 (2014).
[19] P. J. W. Moll, N. L. Nair, T. Helm, A. C. Potter, I. Kimchi, A. Vishwanath, and J. G. Analytis, Nature **535**, 266 (2016).
[20] D. Shoenberg, *Magnetic Oscillations in Metals* (Cambridge University Press, Cambridge, 1984).
[21] F. Guinea, M. I. Katsnelson, and A. K. Geim, Nat Phys **6**, 30 (2010).
[22] N. Levy, S. A. Burke, K. L. Meaker, M. Panlasigui, A. Zettl, F. Guinea, A. H. C. Neto, and M. F. Crommie, Science **329**, 544 (2010).
[23] H. Shapourian, T. L. Hughes, and S. Ryu, Phys. Rev. B **92**, 165131 (2015).
[24] A. Cortijo, Y. Ferreirós, K. Landsteiner, and M. A. H. Vozmediano, Phys. Rev. Lett. **115**, 177202 (2015).
[25] H. Sumiyoshi and S. Fujimoto, Phys. Rev. Lett. **116**, 166601 (2016).
[26] D. Pikulin, A. Chen, and M. Franz, arXiv:1607.01810 (unpublished).
[27] A. G. Grushin, J. W. F. Venderbos, A. Vishwanath, and R. Ilan, ArXiv e-prints (2016), 1607.04268.
[28] L. P. He, X. C. Hong, J. K. Dong, J. Pan, Z. Zhang, J. Zhang, and S. Y. Li, Phys. Rev. Lett. **113**, 246402 (2014).
[29] Y. Liu, C. Zhang, X. Yuan, T. Lei, C. Wang, D. Di Sante, A. Narayan, L. He, S. Picozzi, S. Sanvito, et al., NPG Asia Mater **7**, e221 (2015).
[30] J. Xiong, S. Kushwaha, J. Krizan, T. Liang, R. J. Cava, and N. P. Ong, EPL (Europhysics Letters) **114**, 27002 (2016).
[31] Z. Wang, H. Weng, Q. Wu, X. Dai, and Z. Fang, Phys. Rev. B **88**, 125427 (2013).
[32] S. Borisenko, Q. Gibson, D. Evtushinsky, V. Zabolotnyy, B. Büchner, and R. J. Cava, Phys. Rev. Lett. **113**, 027603 (2014).
[33] M. Neupane, S.-Y. Xu, R. Sankar, N. Alidoust, G. Bian, C. Liu, I. Belopolski, T.-R. Chang, H.-T. Jeng, H. Lin, et al., Nat Commun **5**, 4786 (2014).
[34] S. Jeon, B. B. Zhou, A. Gyenis, B. E. Feldman, I. Kimchi, A. C. Potter, Q. D. Gibson, R. J. Cava, A. Vishwanath, and A. Yazdani, Nat Mater **13**, 851 (2014).
[35] Z. K. Liu, J. Jiang, B. Zhou, Z. J. Wang, Y. Zhang, H. M. Weng, D. Prabhakaran, S.-K. Mo, H. Peng, P. Dudin, et al., Nat Mater **13**, 677 (2014), ISSN 1476-1122.
[36] Z. Wang, Y. Sun, X.-Q. Chen, C. Franchini, G. Xu, H. Weng, X. Dai, and Z. Fang, Phys. Rev. B **85**, 195320 (2012).
[37] Z. K. Liu, B. Zhou, Y. Zhang, Z. J. Wang, H. M. Weng, D. Prabhakaran, S.-K. Mo, Z. X. Shen, Z. Fang, X. Dai, et al., Science **343**, 864 (2014).
[38] Y. Zhang, Z. Liu, B. Zhou, Y. Kim, Z. Hussain, Z.-X. Shen, Y. Chen, and S.-K. Mo, Applied Physics Letters **105**, 031901 (2014).
[39] S.-Y. Xu, I. Belopolski, N. Alidoust, M. Neupane, G. Bian, C. Zhang, R. Sankar, G. Chang, Z. Yuan, C.-C. Lee, et al., Science **349**, 613 (2015).
[40] B. Q. Lv, H. M. Weng, B. B. Fu, X. P. Wang, H. Miao, J. Ma, P. Richard, X. C. Huang, L. X. Zhao, G. F. Chen, et al., Phys. Rev. X **5**, 031013 (2015).
[41] C. Shekhar, A. K. Nayak, Y. Sun, M. Schmidt, M. Nicklas, I. Leermakers, U. Zeitler, Y. Skourski, J. Wosnitza, Z. Liu, et al., Nat Phys **11**, 645 (2015), letter.
[42] L. X. Yang, Z. K. Liu, Y. Sun, H. Peng, H. F. Yang, T. Zhang, B. Zhou, Y. Zhang, Y. F. Guo, M. Rahn, et al., Nat Phys **11**, 728 (2015), letter.
[43] S.-Y. Xu, N. Alidoust, I. Belopolski, Z. Yuan, G. Bian, T.-R. Chang, H. Zheng, V. N. Strocov, D. S. Sanchez, G. Chang, et al., Nat Phys **11**, 748 (2015), article.
[44] H. Li, H. He, H.-Z. Lu, H. Zhang, H. Liu, R. Ma, Z. Fan, S.-Q. Shen, and J. Wang, Nat Commun **7** (2016).
[45] C.-Z. Li, L.-X. Wang, H. Liu, J. Wang, Z.-M. Liao, and D.-P. Yu, Nat Commun **6**, 10137 (2015).
[46] L.-X. Wang, C.-Z. Li, D.-P. Yu, and Z.-M. Liao, Nat Commun **7**, 10769 (2016).
[47] J. Cano, B. Bradlyn, Z. Wang, M. Hirschberger, N. Ong, and B. Bernevig, arXiv:1604.08601 (unpublished).

Model parameters

We model Cd_3As_2 using the Hamiltonian (1) with parameters taken from the first principles band structure calculations [26, 47] and with the lattice constants corresponding to the actual material, $a_{x,y} = 3$Å, $a_z = 5$Å. This implies that the constants used in (2) are: $\Lambda = 0.296$eV, $t_0 = -7.4811$eV, $t_1 = 1.5016$eV, and $t_2 = 3$eV. Additionally, we model the particle-hole asymmetry of the real Cd_3As_2 using

$$\epsilon_{\boldsymbol{k}} = r_0 + r_1 \cos a_z k_z + r_2(\cos a_x k_x + \cos a_y k_y), \quad (10)$$

with $r_0 = 5.9439$eV, $r_1 = -0.8472$eV, and $r_2 = -2.5556$eV.

The results for the dispersion and DOS for the realistic particle-hole asymmetric case are shown in Fig. 5. We note the similarity of the results with those displayed in the main text and in Fig. 5. Specifically, both the real magnetic field B and the strain-induced pseudomagnetic field b give rise to pronounced Landau levels. We thus conclude that all our predictions remain valid for this realistic Dirac semimetal.

Conductivity calculation

First we obtain the analytical expression for the conductivity of Dirac-Landau levels in the bulk and in the continuum limit. From the dispersion relation (9) we obtain the velocity in y direction,

$$v_n^s(k_y) = \frac{1}{\hbar}\frac{\partial E_n^s}{\partial k_y} = s v_y \frac{k_y}{\sqrt{k_y^2 + n\Omega}}, \quad (11)$$

where s is the sign of the energy and $\Omega = \frac{2eB}{\hbar c}\frac{v_x v_z}{v_y^2}$. Then we use the familiar formula for the DC conductivity σ_{yy} due to the n'th Landau level in the relaxation time approximation

$$\sigma_n^s(\mu) = e^2 \int \frac{dk_y}{2\pi} \tau_n^s(E_n^2(k_y))(v_n^s(k_y))^2 \left(-\frac{\partial f(E-\mu)}{\partial E}\right)_{E_n^s(k_y)}. \quad (12)$$

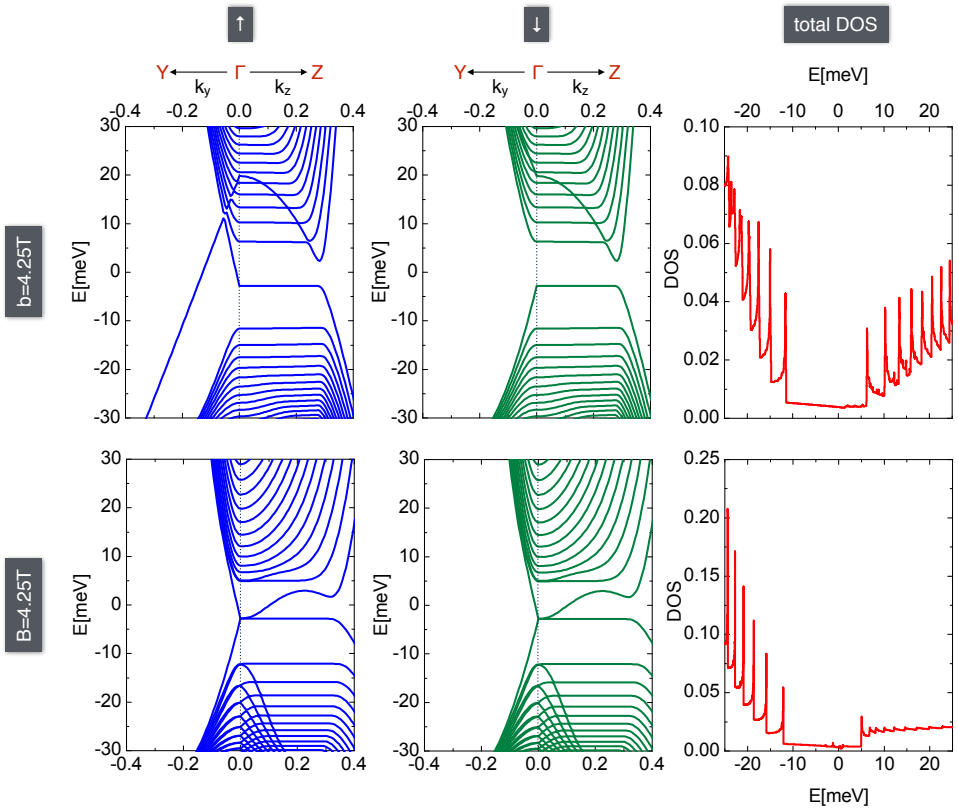

FIG. 5: Bandstructure and density of states for the model of Cd_3As_2 with the particle-hole asymmetric part (10) included. Top row is for the pseudomagnetic field $b = 4.25$T (corresponding to $\alpha = 0.04$, stronger strain than in the main text), and bottom row is for real magnetic field $B = 4.25$T. From left to right – bandstructure for spin up band, bandstructure for spin down band, and normalized total DOS.

Here $f(\epsilon)$ is the Fermi function. We assume zero temperature, angle-independent relaxation time, and substitute the dispersion relation to obtain

$$\sigma_n^s(\mu) = e^2\tau_n^s \int \frac{dk_y}{2\pi} \frac{v_y^2 k_y^2}{k_y^2 + n\Omega} \delta(E_n^s(k_y) - \mu). \qquad (13)$$

After the change of the integration variable from k_y to $E_n^s(k_y)$ and integration we find

$$\sigma_n^s(\mu) = \frac{e^2\tau_n^s v_y}{\hbar\pi} \left. \frac{\mathrm{Re}\sqrt{E_n^2 - n\hbar^2 v_y^2\Omega}}{E_n^s} \right|_{E_n^s=\mu}, \qquad (14)$$

and the total conductivity is

$$\sigma = \frac{2e^2 v_y}{h} \sum_n \tau_n(\mu) \mathrm{Re}\sqrt{\frac{\mu^2 - n\hbar^2 v_y^2\Omega}{\mu^2}}. \qquad (15)$$

Finally, we estimate the relaxation time in the lowest order Born approximation

$$\frac{1}{\tau} = 2\pi D(\mu) n_{\mathrm{imp}} C, \qquad (16)$$

where $D(\mu)$ is the density of states at the Fermi level and n_{imp} is the impurity concentration. Constant C depends on the details of scattering from impurities. Thus the final formula we use for the conductivity computation in Fig. 4 is

$$\sigma_{yy} = \frac{e^2 v_y}{\pi\hbar D(\mu) n_{\mathrm{imp}} C} \sum_n \mathrm{Re}\sqrt{\frac{\mu^2 - n\hbar^2 v_y^2\Omega}{\mu^2}}. \qquad (17)$$

Numerically we use the same formula (12), but input the actual velocities and energies into it.

Quantum oscillations above Lifshitz transition

In this section we present the results for QO at energy 28meV, above the Lifshitz transition (at approximatly 20meV). In Fig. 6a we see that the area of the Fermi surface causing the oscillations in B and b fields is different by slightly larger than a factor of 2. For the external magnetic field case the effective area of the Fermi surface is approximately doubled as compared to the gauge field. Strain couples only to the linear part of the Hamiltonian as a gauge field, therefore only the

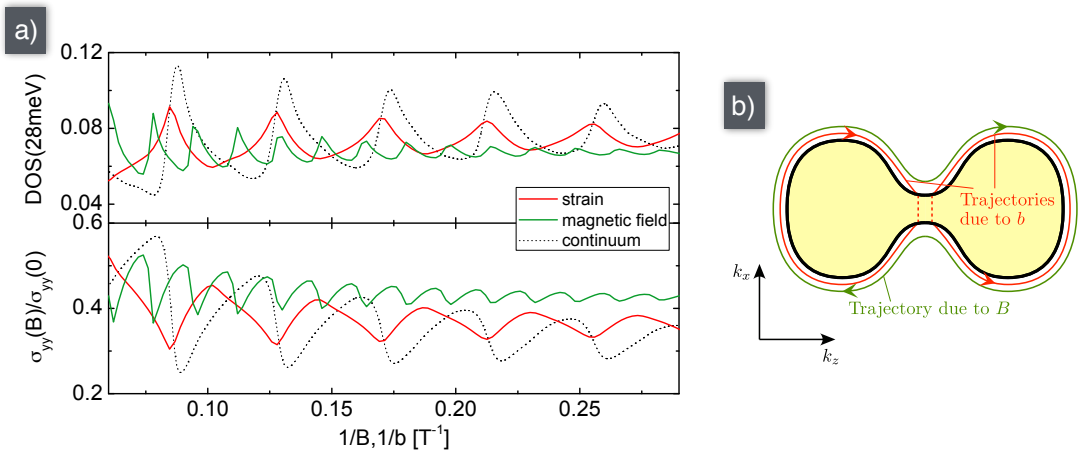

FIG. 6: a) QO above the Lifshits transition due to ordinary magnetic field and due to the gauge field. Period difference by more than a factor of 2 is seen. The low-energy analytics does not apply anymore, as expected. b) Corresponding hypothesized quasiclassical trajectories of electrons in the Brillouin zone. Green – for B_y field, and red – for b_y field.

oscillations around each of the Weyl points are possible. Notice also that the electron in the pseudmagnetic field travels clockwise around one of the Weyl points and counterclockwise around the another. The precise nature of the corresponding quasiclassical trajectories above the Lifshitz transition is therefore an interesting open question which we leave for further study. We speculate that they include tunneling between the opposite points of the Fermi surface as depicted in Fig. 6b. Such trajectories would define an extremal area consistent with our numerical results.

Equivalence of external and gauge fields

In this section we additionally substantiate the proposed equivalence of b and B fields and suggest an additional experimental test. We propose to apply external magnetic field of fixed strength and then slowly turn on strain (or vice versa, whichever is more convenient in a particular experimental design). This will result in splitting of the first peak in DOS as seen in Fig. 7. This happens because the two Weyl cones will feel different effective magnetic fields, $B + b$ and $B - b$, which result in two independent sequences of peaks in DOS. Observation of the splitting would prove the identical nature of the gauge and external magnetic fields in each of the Weyl cones, and establish that the two cones feel opposite effective field due to b.

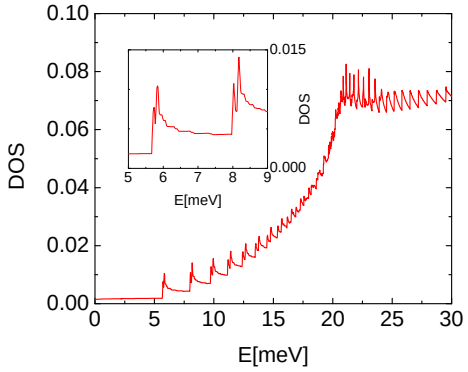

FIG. 7: Normalized density of states for both fields present, $B = 1\text{T}$ and $b = 0.0184\text{T}$. Each of the DOS peaks due to ordinary magnetic field splits due to torsion thus proving the equivalence of the external and gauge fields. Inset gives closer view of the first two peaks.